Article

Current Biology

Mapping Load-Bearing in the Mammalian Spindle Reveals Local Kinetochore Fiber Anchorage that Provides Mechanical Isolation and Redundancy

Graphical Abstract

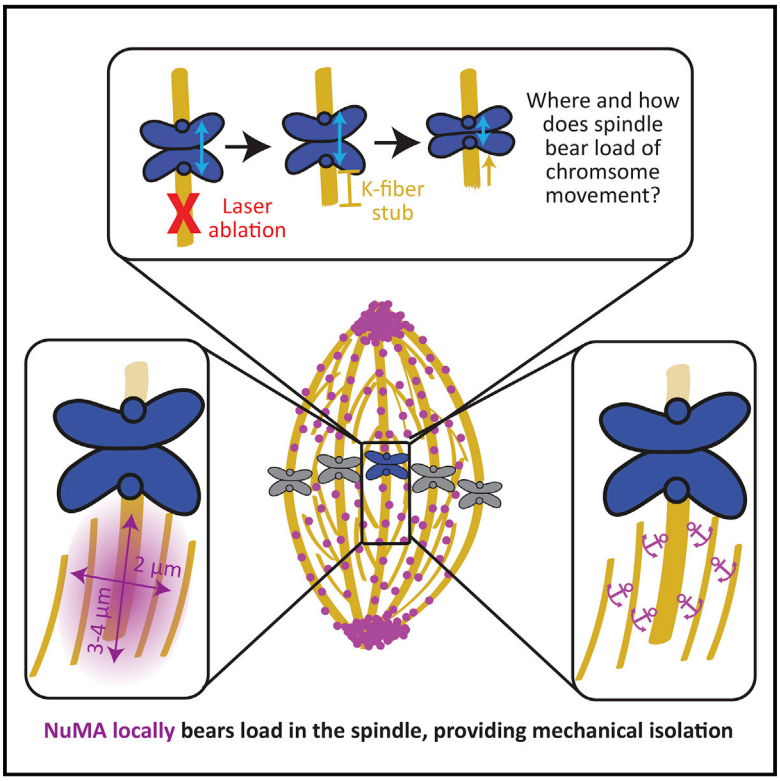

Highlights

- Mammalian spindle locally and redundantly bears load of chromosome movement
- Load-bearing scales along first 3–4 μm of k-fibers and occurs within ~2 μm laterally
- Post-ablation relaxation suggests that microtubule crosslinks can bear load dynamically
- NuMA is required for local load-bearing in the spindle, but Eg5 and PRC1 are not

Authors

Mary Williard Elting, Manu Prakash, Dylan B. Udy, Sophie Dumont

Correspondence

sophie.dumont@ucsf.edu

In Brief

To move chromosomes, the spindle must robustly hold on to kinetochore fibers. Elting et al. show that the mammalian spindle locally bears this load near kinetochores and map how it propagates in space-time. They identify NuMA crosslinks as local load-bearers and suggest that these could provide both spindle mechanical redundancy and adaptability.

Elting et al., 2017, Current Biology 27, 1–11
July 24, 2017
http://dx.doi.org/10.1016/j.cub.2017.06.018

CellPress

Please cite this article in press as: Elting et al., Mapping Load-Bearing in the Mammalian Spindle Reveals Local Kinetochore Fiber Anchorage that Provides Mechanical Isolation and Redundancy, Current Biology (2017), http://dx.doi.org/10.1016/j.cub.2017.06.018

Current Biology
Article

Mapping Load-Bearing in the Mammalian Spindle Reveals Local Kinetochore Fiber Anchorage that Provides Mechanical Isolation and Redundancy

Mary Williard Elting,[1] Manu Prakash,[2] Dylan B. Udy,[1,4] and Sophie Dumont[1,3,5,*]
[1]Department of Cell and Tissue Biology, University of California, San Francisco, San Francisco, CA 94143, USA
[2]Department of Bioengineering, Stanford University, Stanford, CA 94305, USA
[3]Department of Cellular and Molecular Pharmacology, University of California, San Francisco, San Francisco, CA 94143, USA
[4]Present address: MCB Graduate Program, University of Washington, Seattle, WA 98195, USA
[5]Lead Contact
*Correspondence: sophie.dumont@ucsf.edu
http://dx.doi.org/10.1016/j.cub.2017.06.018

SUMMARY

Active forces generated at kinetochores move chromosomes, and the dynamic spindle must robustly anchor kinetochore fibers (k-fibers) to bear this load. The mammalian spindle bears the load of chromosome movement far from poles, but we do not know where and how—physically and molecularly—this load distributes across the spindle. In part, this is because probing spindle mechanics in live cells is difficult. Yet answering this question is key to understanding how the spindle generates and responds to force and performs its diverse mechanical functions. Here, we map load-bearing across the mammalian spindle in space-time and dissect local anchorage mechanics and mechanism. To do so, we laser-ablate single k-fibers at different spindle locations and in different molecular backgrounds and quantify the immediate relaxation of chromosomes, k-fibers, and microtubule speckles. We find that load redistribution is locally confined in all directions: along the first 3–4 μm from kinetochores, scaling with k-fiber length, and laterally within ~2 μm of k-fiber sides, without detectable load sharing between neighboring k-fibers. A phenomenological model suggests that dense, transient crosslinks to the spindle along k-fibers bear the load of chromosome movement but that these connections do not limit the timescale of spindle reorganization. The microtubule crosslinker NuMA is needed for the local load-bearing observed, whereas Eg5 and PRC1 are not detectably required, suggesting specialization in mechanical function. Together, the data and model suggest that NuMA-mediated crosslinks locally bear load, providing mechanical isolation and redundancy while allowing spindle fluidity. These features are well suited to support robust chromosome segregation.

INTRODUCTION

When mammalian cells divide, depolymerizing microtubules generate forces at kinetochores to move chromosomes and ultimately segregate them. Microtubule bundles called kinetochore fibers (k-fibers) attach to kinetochores; thus, equal and opposite forces are exerted on kinetochores by k-fibers and on k-fibers by kinetochores, in accord with Newton's third law (Figure 1A). However, for chromosomes—rather than k-fibers—to move, k-fibers must anchor to the spindle to bear the load of chromosome movement [1]. How the mammalian spindle robustly anchors k-fibers and segregates chromosomes despite its dynamic and flexible nature remains unclear. Yet, answering this question is key to understanding how the spindle generates and responds to force and thus to determining how the cell moves chromosomes and regulates their attachment and segregation.

In one model, k-fibers are anchored at spindle poles and their microtubules are tensed all along their lengths [2–4]. However, k-fibers can bear load and support chromosome movement without being directly connected to the pole or other k-fibers in both mammalian [5, 6] and insect cells [7]. These observations support a model where k-fibers are anchored along their lengths: in this model, different sections of the k-fibers can be under different forces [5, 8] and "traction force" may [9] or may not [10] be proportional to k-fiber length.

The physical and molecular bases of k-fiber anchorage in the spindle body are poorly understood. The local physical environment around a k-fiber dictates how kinetochore forces are distributed in space and time across the spindle; yet, whereas directly probing local mechanics has become possible in spindles that can be reconstituted in extract [11, 12], such perturbation remains challenging in mammalian cells. Although we do not know what structure k-fibers anchor to, spindle microtubules connecting to k-fibers [13] are a clear candidate. These connecting microtubules could, for example, include interpolar microtubules [8, 14, 15], such as "bridging fiber" microtubules [5], or neighboring k-fibers connecting through minus ends [16, 17]—or other mechanisms could be responsible [18]. A further challenge is that, if the spindle laterally bears load, it must do so using an anisotropic spindle material that is weaker along its lateral

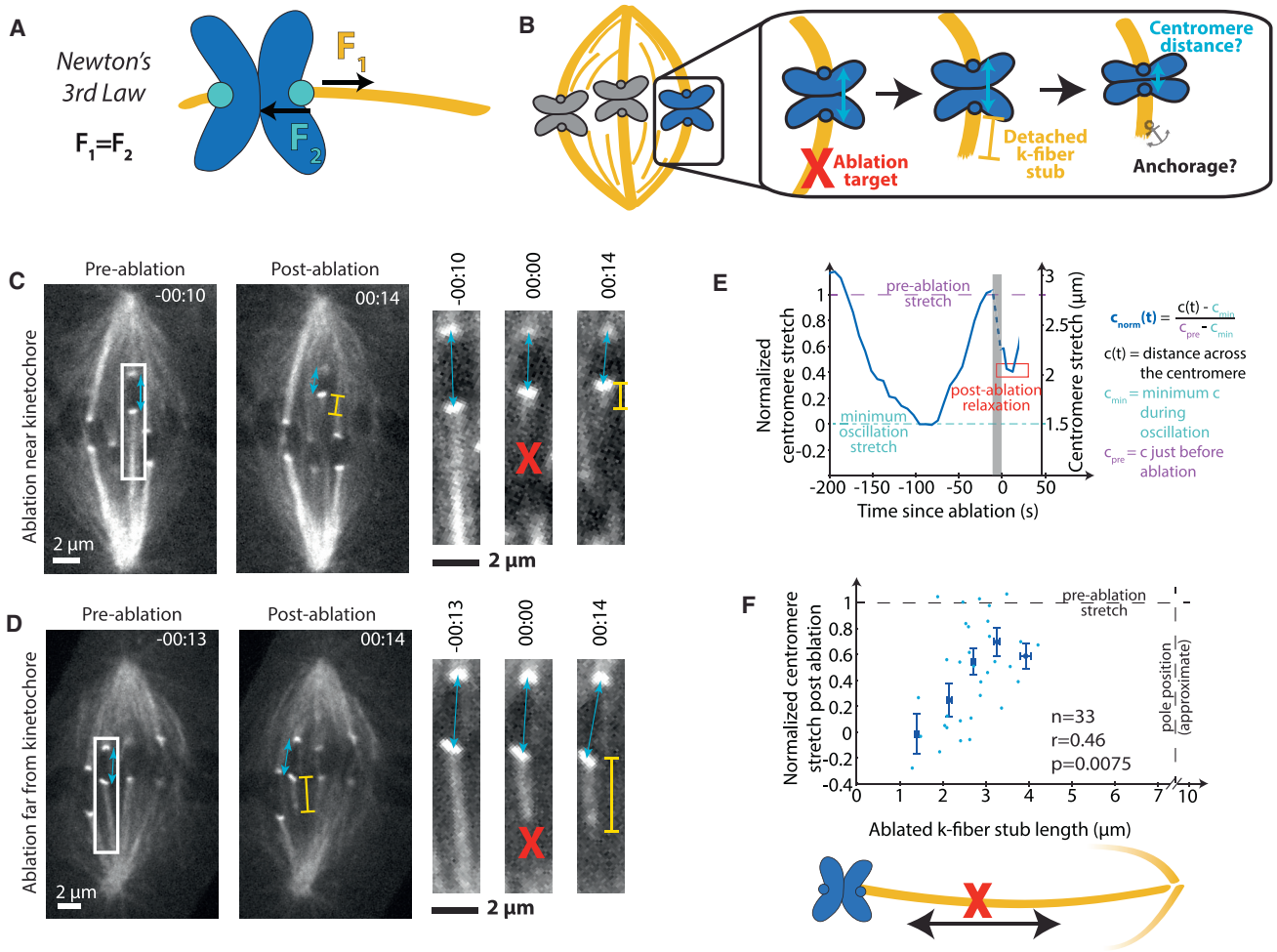

Figure 1. The Load of Chromosome Movement Is Borne Proportionally along the First 3–4 µm of the K-Fiber

(A) Equal and opposite forces pull on kinetochores (cyan) and k-fibers (yellow).

(B) Cartoon of ablation assay to map where the spindle bears load along the k-fiber. Centromere stretch that remains after ablation indicates residual force on the k-fiber stub.

(C) Live confocal imaging of PtK2 cell expressing EYFP-Cdc20 and EGFP-α-tubulin. Time since ablation, min:s. Representative example showing that, when we ablate (red X) near kinetochores, the centromere (blue arrow) relaxes (inset), indicating decreased load-bearing ability by the short k-fiber stub (yellow bar).

(D) Imaging as in (C), representative example showing that after ablation far from kinetochores, the centromere remains stretched, indicating preserved load-bearing ability by the long k-fiber stub.

(E) Representative plot of centromere stretch over time before and after ablation, normalized as defined on a per-trace basis (see STAR Methods).

(F) Normalized centromere stretch post-ablation versus k-fiber stub length of individual measurements (light blue dots) and binned data (darker, larger dots; error bars SEM). The correlation is significant ($p = 0.0075$), and its moderate coefficient ($r = 0.46$) likely reflects both cell-to-cell variation and the plateau at long stubs. See also Movies S1 and S2.

axis [8, 11, 13, 19–21]. The first identification herein of a molecule whose absence changes the spindle's load-bearing map is an important step toward uncovering the mechanisms that bear load—and understanding how they support the mechanical integrity and dynamics essential to accurate chromosome segregation.

Here, we combine targeted k-fiber laser ablation and quantitative imaging to build a map of where the mammalian spindle bears the load of chromosome movement and to probe the mechanics and molecular basis of the underlying anchorage. We find that effective anchorage is proportional to length in the first few µms of a k-fiber but does not require the entire length from kinetochore to pole and that neighboring k-fibers do not apparently share the load. The data support a model where spindle connections linearly distributed along k-fibers bear load but where the viscosity of these connections does not limit the timescale of spindle reorganization. We find that depleting the microtubule crosslinker NuMA decreases local load-bearing, whereas inhibition or depletion of other molecules linking microtubules, Eg5 and PRC1, do not. This dynamic and local nature of load-bearing is well suited for making chromosome movement robust to spindle reorganization and for spatially confining the impact of structural spindle defects.

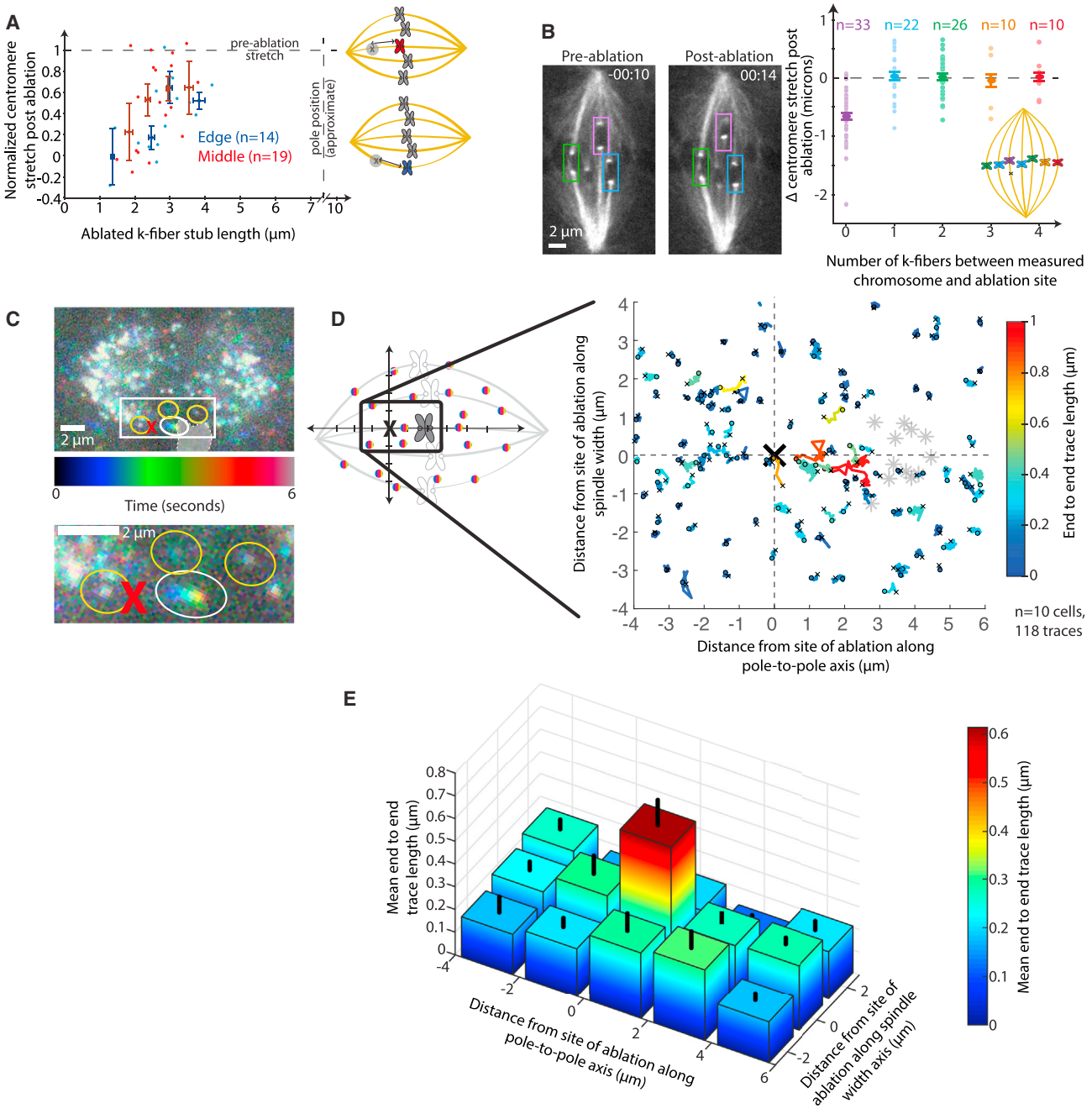

Figure 2. The Load of Kinetochore Forces Is Borne Laterally within ~2 μm of K-Fibers

(A) Normalized centromere stretch versus k-fiber stub length of individual measurements (light dots) and binned data (darker, larger dots; error bars SEM) for chromosomes on the edge (blue) and in the center (red) of the spindle with same source data as Figure 1F.

(B) Left: representative live-imaged PtK2 cell (same cell as in Figure 1C) diagramming neighboring chromosomes. Time since ablation, min:s. Right: change in centromere stretch following ablation for ablated k-fiber (purple) and increasingly distant neighboring k-fibers across the spindle is shown (blue, green, orange, and red, as in cartoon). Individual measurements are lighter dots. Binned data, with SEM error bars, are larger dots.

(C) Live confocal movie of PtK2 cell expressing SunTag-rigor kinesin speckles at a fast timescale (~300 ms), projected into a single plane colored with time, with box indicating inset region below. A speckle on the ablated k-fiber (white circle) appears as a rainbow going from blue to orange because it relaxes a significant distance during the movie, whereas nearby speckles (e.g., yellow circles) do not move and thus appear in more uniform color. Chromosome position at first frame is indicated by shaded region with dotted outline.

(D) Individual speckle tracks (colored by their end-to-end distance; n = 118 speckles from ten cells) and chromosomes whose k-fibers were targeted (gray stars, one per cell) are shown superimposed and aligned, with orientation as in cartoon (see STAR Methods). The majority of long speckle traces (warm colors)

(legend continued on next page)

RESULTS AND DISCUSSION

The Load of Chromosome Movement Is Borne Proportionally along the First 3–4 μm of the K-Fiber

To map where along their lengths k-fibers bear the load of chromosome movement in mammalian spindles, we used laser ablation to sever k-fibers at varying distances from the kinetochore (Figure 1B). We visualized both microtubules and kinetochores (EGFP-α-tubulin and EYFP-Cdc20, respectively) in PtK2 cells using confocal imaging. These cells have k-fibers whose microtubules largely extend from kinetochore to pole [22] and have few chromosomes, allowing us to effectively target individual k-fibers. We began by measuring the response of the chromosome because, at metaphase, forces at kinetochores stretch centromeres and are opposed by k-fiber anchorage in the spindle. Thus, high residual centromere stretch after ablation reflects strong anchorage on the remaining k-fiber stub, whereas low residual stretch indicates weak anchorage. We ablated k-fibers at times of maximal centromere stretch to maximize the dynamic range of the assay and examined the new steady-state centromere distances with ablated, detached k-fiber stubs. This new, brief steady state occurred before the ablated k-fiber stubs were pulled poleward by dynein [16, 17].

We systematically ablated k-fibers from 1 to 4 μm from kinetochores and mapped how centromere relaxation changed with ablation position. The centromere relaxed when ablation was near the kinetochore (Figure 1C; Movie S1) and remained stretched when ablation was farther from the kinetochore but also far from poles (Figure 1D; Movie S2). This observation is in qualitative agreement with previous work in mammalian cells [5, 6] and indicates that long k-fiber stubs remained anchored following ablation, without a direct connection to the pole or other k-fibers. However, here, we see a considerable drop in centromere stretch for stubs as long as 2–3 μm, suggesting that load is borne gradually over a few μms. The normalized centromere distance (Figure 1E) to which each chromosome relaxed correlated with the distance from the kinetochore to the ablation site ($r = 0.46$; $p = 0.0075$; $n = 33$; Figure 1F). Ablating a single k-fiber, maximizing the dynamic range of our assay, and normalizing for centromere variability are likely key to revealing how load is distributed along k-fiber lengths. The apparent linear relationship, which occurs for stubs between ~1 and ~3 μm in length, suggests that load-bearing along the k-fiber stub scales with its length. However, this relationship plateaus: for stubs at least 3–4 μm in length, we observed little relaxation following ablation. Further, k-fiber stubs of <~1.5 μm were not able to generate sufficient load to stretch the centromere beyond its minimal metaphase distance. The relaxation response we observe is both rapid and length dependent and thus unlikely to be mediated by dynein pulling on new minus ends, which takes longer to engage and is length independent [16]. Together, the data are consistent with a constant number of molecular-scale force generators per unit length, which bear load locally, in the first 3–4 μm near the kinetochore, and inconsistent with a single anchor point at a fixed distance from the kinetochore.

The Load of Kinetochore Forces Is Borne Laterally within ~2 μm of K-Fibers

To probe how the load of chromosome movement is distributed in the spindle body, we mapped load sharing along the lateral spindle axis. In *Drosophila* S2 cells, where chromosomes do not oscillate at metaphase, the spindle distributes load between neighboring chromosomes [14]; whether such force distribution might also apply in mammalian cells [23], where chromosomes oscillate at metaphase, is less clear. We reasoned that, if lateral anchorage distributed significant load between neighboring k-fibers, we should see less effective anchorage of k-fibers at the spindle edge, which have fewer neighbors, compared to those in the spindle center, which have more neighbors. We separated the previous dataset (Figure 1F) into "edge" and "center" k-fibers and could not detect a significant difference in centromere relaxation after ablation in these two populations (Figure 2A; $n = 14$ and 19, respectively). This similarity in behavior suggests that lateral load-bearing also occurs locally.

To further test whether neighboring k-fibers shared their load, we ablated a single k-fiber and examined the responses of centromeres of neighboring chromosomes following ablation. Although variability in neighboring centromere stretch at the time of ablation may limit the sensitivity of this measurement, if significant force was distributed between k-fibers, we would expect that cutting one k-fiber would decrease the anchorage of neighboring k-fibers, causing relaxation of their centromeres. From distant k-fibers to nearest neighbor k-fibers, we could not detect a significant decrease in centromere stretch following ablation (Figures 2B and S1A; $n = 68$). This observation too suggests that the load of k-fiber anchorage is distributed over a shorter distance than the distance between neighboring k-fibers (~2 μm) and, thus, that spindle structures located in between these k-fibers must bear the load of chromosome movement. This result is consistent with prior measurements that found small correlations between the movements of neighboring human chromosomes [18]: neighboring k-fibers are closer in human cells, so these correlations may result from mechanical coupling over distances comparable to where we see relaxation or from chromosome/chromosome (rather than k-fiber/k-fiber) interactions. Whereas we do not detect mechanical coupling of neighboring k-fibers in the spindle body, there may be coupling that is too weak for us to detect. When significantly larger forces were previously used to pull chromosomes away from the metaphase plate via microneedles in insect cells, neighboring k-fibers exhibited coupled movement [13], and we also expect that k-fibers become more coupled near poles.

To directly map how microtubules across the whole spindle mechanically respond to local changes in architecture and force, we imaged microtubule speckles at high time resolution (~300 ms) after k-fiber laser ablation. We sparsely labeled

representing significant relaxation are between the site of ablation and the chromosome, whereas speckles >~2 μm laterally away from the site of ablation typically only move short distances (cool colors). Small "o" indicates beginning of each trace, and small "x" indicates end.

(E) Subset of data from (D), plotted as binned means and SEM of end-to-end trace length as a function of distance along both spindle axes. Central bin from $x = 0$ to 2 μm and $y = -1$ to 1 μm has significantly higher mean than the surrounding eight bins ($n = 9$ in center bin; $n = 39$ total in surrounding bins; $p = 2 \times 10^{-5}$). See also Figure S1 and Movie S3.

microtubules by expressing a Sun-tagged truncated kinesin-1 mutant that rigor binds to microtubules [24]. This bright, single-molecule imaging method allowed us to visualize the movement of microtubules with respect to each other (Figure 2C; Movie S3), and by pooling the data over many such experiments, we created a map of where relaxation occurred (Figures 2D and 2E; n = 118 speckles in ten cells). Whereas most of the speckles we detected were apparently localized along k-fibers, we also detected speckles that do not appear to colocalize with k-fibers (Figures S1B and S1C) and thus may be on non-k-fiber microtubules. After ablation, speckles apparently located on the ablated k-fiber moved away from the ablation site at similar speeds to whole k-fibers. Speckles within a bin 2 μm wide and along the first 2 μm toward the chromosome from the ablation site relaxed farther than those in the pooled surrounding eight bins of the same size (Figure 2E; n = 8 near speckles and 39 farther speckles; $p = 2 \times 10^{-5}$). Most of the moving speckles colocalized with ablated k-fibers (Figures S1B and S1C). Though dim SiR-tubulin imaging made it difficult to definitively categorize all speckles as localizing to k-fibers or not, some speckles that relaxed did not appear to colocalize with k-fibers (Figures S1B and S1C) and, as such, may be on non-k-fiber microtubules. Speckles farther away had no detectable movement.

Thus, k-fibers appear not only mechanically isolated from neighboring k-fibers but also from non-k-fiber microtubules more than ~2 μm away. Relaxation of nearby speckles adjacent to the ablated k-fiber is consistent with these k-fibers anchoring to neighboring non-k-fiber microtubules, though because we cannot directly visualize non-k-fiber microtubules, we cannot definitively classify them as such. In turn, the fixed appearance of speckles farther away suggests that spindle deformations do not propagate far across the spindle and do not undermine its overall microtubule architecture. Together, the data suggest that this mechanical isolation is, in part, accomplished by a spindle structure that propagates stresses and strains predominately along a pole-to-pole, rather than a lateral, axis and does so locally.

K-Fiber Post-ablation Relaxation Dynamics and Steady State Support a Viscoelastic Model of the Connection of the K-Fiber to the Spindle

To probe the mechanics of the connections between k-fibers and the spindle—the local spindle environment a k-fiber experiences—we asked how relaxation dynamics following ablation varied with k-fiber stub length. We imaged at faster time resolution (~300 ms) than in Figure 1 and used PtK2 GFP-tubulin cells, as they provide good imaging contrast during fast imaging despite photobleaching. We tracked the kinetochore ends of the k-fiber stubs over time (Figure 3A; Movie S4). Most of the relaxation responses we observed fit well to single exponentials (timescales τ; Figure 3B). An exponential form is consistent with viscoelastic relaxation, and smooth relaxation is consistent with many weak interactions, rather than a few strong ones, anchoring k-fibers. We did not observe a significant correlation between the lengths of the k-fiber stubs and the timescales of centromere relaxation (Figure 3C; r = 0.17; p = 0.6; n = 12); similarly, previous results with only short stubs also found that relaxation of the kinetochore itself did not depend on stub length [25].

To project our observations of the post-ablation relaxation dynamics (Figure 3C) and steady state (Figure 1F) onto a framework for local anchorage mechanics, we built a simple phenomenological model and asked whether it was sufficient to recapitulate the main qualitative features of the data (Figure 3D). This model provides a physical intuition for key factors that dominate the relaxation we observe (see STAR Methods for details).

After ablation, the main spindle structural response is that of the centromere, along with the ablated k-fiber stub, relaxing toward the uncut sister k-fiber. Because viscosity cannot alone bear steady-state load, the observation that long stubs can bear load (Figure 1F) indicates that there must be crosslinkers between the k-fiber and spindle. In turn, the non-zero relaxation time (Figure 3C) indicates that at least one of the relaxing structures has a relevant viscous component. Thus, even the simplest model should account for viscoelastic material properties of both the centromeres and the k-fiber-to-spindle connections. To include both the elasticity and viscosity of the relaxing centromere, we model it as a Kelvin-Voigt solid [26]. Finally, we hypothesized that both elastic and viscous connections of the k-fiber to the spindle scale with k-fiber stub length. To model the frictional interaction of the k-fiber stub of known length with the spindle environment, we include a stub-length-dependent viscous drag force. To account for transient binding crosslinkers between the k-fiber and the spindle environment, we include a stub-length-dependent number of what we call "on/off bonds" that rupture at a particular force.

We assume no active response (e.g., spindle repair) during the short timescale observed. Pre-ablation, the system is in a stretched state, with the amount of stored stress indicated by the distance across the centromere. Post-ablation, the system relaxes with a timescale resulting from drag on the k-fiber stub and dissipation in the contracting chromosome. The change in distance across the centromere in response to ablation is equal to the distance moved by the k-fiber stub, which we assume is stiff. Thus, matching the stresses (σ) on the centromere (left) and the k-fiber stub (right), we obtain

$$\sigma = -k_{cent}\Delta x_{cent} - \eta_{cent}\frac{d(\Delta x_{cent})}{dt} = -N_0 L f_0 + L\eta_{MT}\frac{d(\Delta x_{cent})}{dt}, \quad \text{(Equation 1)}$$

where k_{cent} is the centromere stiffness, Δx_{cent} is the extension of the centromere (beyond its rest length), N_0 is the density of k-fiber-to-spindle crosslinks per unit length, L is the k-fiber stub length, f_0 is the maximum force generated per crosslink, η_{MT} accounts for viscous drag (per unit length) of the k-fiber stub in the spindle environment, and η_{cent} is the viscosity of the centromere. Simplifying,

$$-k_{cent}\Delta x_{cent} = -N_0 L f_0 + (L\eta_{MT} + \eta_{cent})\frac{d(\Delta x_{cent})}{dt}. \quad \text{(Equation 2)}$$

The solution to this equation (Figure 3E) is given by

$$\Delta x_{cent}(t) = \begin{cases} \Delta x' + Ae^{-\frac{t}{\tau}}, \ when\ L < L_0 \\ \Delta x_0, \ when\ L \geq L_0 \end{cases}, \quad \text{(Equation 3)}$$

where

$$A = \Delta x_0 - \Delta x'; \ \tau = \frac{L\eta_{MT} + \eta_{cent}}{k_{cent}}; \ L_0 = \frac{k_{cent}\Delta x_0}{N_0 f_0}; \text{ and } \Delta x' = \frac{N_0 L f_0}{k_{cent}}.$$

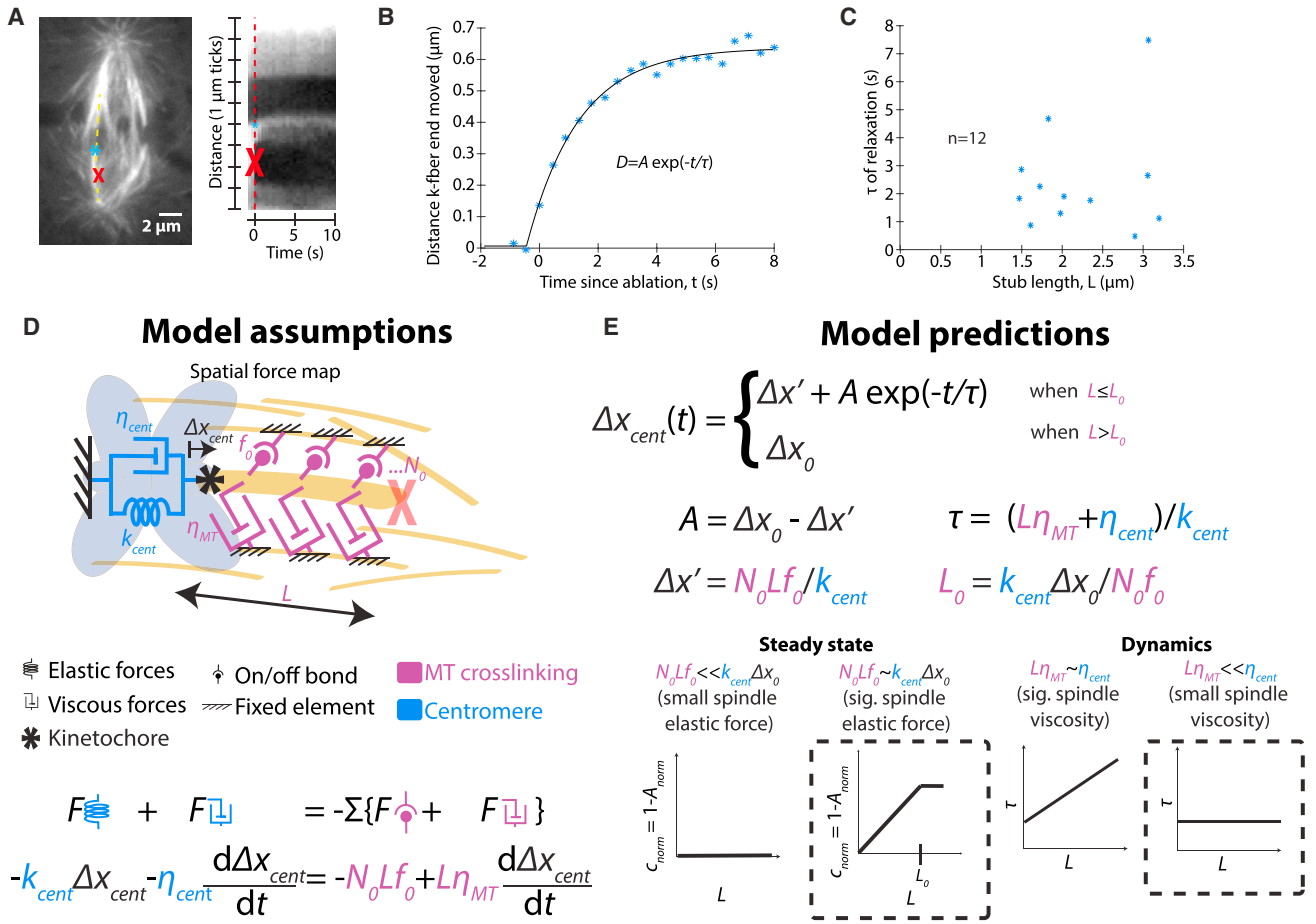

Figure 3. K-Fiber Post-ablation Relaxation Dynamics and Steady State Support a Viscoelastic Model of the Connection of the K-Fiber to the Spindle

(A) Live confocal image immediately before ablation (at red X) of PtK2 cell expressing EGFP-α-tubulin. Kymograph (right) along a k-fiber (yellow dotted line) of imaging at fast time resolution (~300 ms) shows the relaxation process of the tracked k-fiber end (blue *).

(B) Tracking of relaxing k-fiber stub shown in (A) over time, with fit to an exponential relaxation.

(C) Timescales of relaxation (from exponential fits) as a function of stub length (r = 0.17; p = 0.6; n = 12), with undetectable correlation.

(D) Model of viscoelastic forces on k-fiber stubs due to microtubule (MT) crosslinking (magenta) and centromere (blue) and corresponding equation of motion (see Equation 2 in text).

(E) Solved equation of motion for relaxation of k-fiber post-ablation (top; see Equation 3 in text) and cartoons of predicted contributions of model parameters (bottom). Steady-state data showing a linear relationship between the steady-state magnitude of relaxation (*A*) and stub length (*L*) (Figure 1F) are consistent with model parameters predicting that the spindle elastic forces that are proportional to k-fiber length significantly contribute to force balance. Dynamic data that observed τ's do not correlate with stub length (Figure 3C) are consistent with model parameters predicting that viscous forces on k-fibers from their crosslinks to the spindle do not limit the timescale of relaxation, resulting in a timescale (τ) that is independent of *L*.

See also Movie S4.

Here, *A* describes the relaxation magnitude, τ describes its timescale, Δx_0 is the extension of the centromere at the time of ablation, L_0 is the stub length that can sustain the extension Δx_0, and $\Delta x'$ is the extension that can be sustained by a stub of length *L*. Equation 3 qualitatively describes the main features of the dynamic and steady-state relaxation we observe following ablation: the magnitude *A* scales linearly with k-fiber stub length *L* until it plateaus (Figure 1F), and the relaxation follows single-exponential kinetics (Figure 3B). The lack of correlation between the timescale of relaxation and stub length (Figures 3C and 3E) suggests that the timescale of k-fiber movement in the spindle is dominated by centromere viscosity rather than viscous drag from the k-fiber-to-spindle connections, because the latter is expected to depend on stub length (Figure 3E). If there is length-dependent viscosity (friction) between the k-fiber and rest of the spindle that significantly contributes to relaxation, we could not detect it among variation in measured τ's, which may be a consequence of variation in material properties across centromeres. Together, the data suggest that k-fiber-to-spindle crosslinker bonds bear load in a k-fiber length-dependent manner, with longer microtubules more resistant to spindle deformation than short ones. Yet, the data suggest that k-fiber-to-spindle frictional connections do not limit the timescale for local k-fiber and spindle reorganization after acute spindle architectural changes, perhaps because they act on a shorter timescale. Thus, the local environment around a k-fiber is able to bear

load yet fluid. The transient, dynamic nature of crosslinkers that would bear load until catastrophic detachment above a maximum sustainable force is compatible with this spindle property.

NuMA-Mediated Microtubule Crosslinking Locally Bears the Load of Chromosome Movement in the Spindle Body

Non-k-fiber microtubules are a clear candidate structure to which k-fibers may anchor and share load: they are present [15] in the region where we map that load-bearing occurs (Figures 1 and 2); they rapidly turnover [27], which would facilitate spindle reorganization; and they are mechanically connected to k-fibers [13]. We first tested whether increased microtubule-microtubule crosslinking led to more local load-bearing in the spindle. To do so, we increased crosslinking by treating cells with 2-(1-(4-fluorophenyl)cyclopropyl)-4-(pyridin-4-yl)thiazole (FCPT), which rigor binds the motor Eg5 to microtubules [28]. Eg5 localizes throughout the spindle [29], including in the vicinity where we observe local load-bearing, and functions as a microtubule slider and crosslinker [30]. We treated cells with concentrations of FCPT sufficient to decrease microtubule flux (Figures S2E and S2E'; STAR Methods), indicating increased microtubule crosslinking, but that did not grossly perturb spindle structure or dynamics, allowing chromosomes to still move (Movie S5; Figure S2A). Under these conditions, we measured centromere stretch after ablation near the kinetochore, because short stubs yield a larger dynamic range for measuring an increased ability to bear load. We observed decreased centromere relaxation following near-kinetochore ablation in FCPT (n = 10; Figures 4A and 4A'; Movie S5), which demonstrates that increased microtubule-microtubule crosslinking is capable of increasing k-fiber anchorage and making load-bearing even more local.

Given that microtubule crosslinking is able to locally anchor k-fibers, we next asked whether key spindle microtubule crosslinkers played essential roles in locally bearing load along k-fibers. This time, we focused on ablation far from the kinetochore, where the significant load-bearing by a longer stub gave the greatest dynamic range for detecting a decreased ability to bear load. We first examined the role of the active force generator Eg5, which, in addition to its crosslinking role, exerts outward force in the spindle [31] and has been previously reported to mechanically connect neighboring chromosome movements [18]. When we examined bipolar spindles treated with S-trityl-L-cysteine (STLC) [32], which causes Eg5 to release from microtubules, we saw no effect on the k-fiber's load-bearing ability (n = 9; Figures 4B and S2B; Movie S6). Thus, whereas Eg5 is capable of increasing the density at which load-bearing force is generated when its microtubule affinity is increased, it is not essential for local load-bearing in the spindle body.

Second, we examined the role of the passive microtubule crosslinker PRC1, which bundles microtubules in the center of the spindle where local load-bearing occurs. It has a reported role specifically in "bridging fibers" [5] whose geometry—connecting sister k-fibers by spanning the centromere [33]—is well-suited to maintaining poleward force on chromosomes [15, 34]. Furthermore, overexpression of PRC1 and concomitant thickening of bridging fibers results in a greater angular deflection of the centromere following ablation in HeLa cells [5]. However, following depletion of PRC1 by RNAi [35], which was verified by immunofluorescence (Figures S2G and S2G'; STAR Methods), we did not detect any effect on local k-fiber load-bearing in PtK2 cells (n = 10; Figures 4C and S2C; Movie S7), indicating that wild-type levels of PRC1 are not essential for local load-bearing. Thus, whereas PRC1-mediated bridging microtubules can effectively stiffen the centromere [5], our results suggest they may not significantly bear the load of stretching it. In HeLa cells, PRC1 knockdown leads to an ~10% reduction in interkinetochore distance [33]: there may be species-specific differences, and because this is a steady-state measurement, it may or may not report on the same underlying mechanics as those we measure following ablation.

Finally, we examined a role for NuMA, a microtubule crosslinker that stabilizes spindle poles [3], where it primarily localizes, but that also localizes diffusely throughout the spindle body, including on k-fibers [36] (Figure S2H), where it is uniformly present in the first ~3 μm of k-fibers (Figure S2F). Because complete NuMA depletion significantly perturbs spindle structure, making it difficult to differentiate between a direct or indirect role of NuMA in load-bearing, we focused on cells that exhibited only mild phenotypes of NuMA knockdown, such as mildly splayed poles or slightly detached centromeres (Movie S8; Figure S2D; STAR Methods). We verified knockdown in phenotypically similar cells by immunofluorescence (Figures S2H and S2H'; STAR Methods). Strikingly, even these cells displayed a decrease in local load-bearing for long k-fiber stubs (n = 16; Figures 4D, 4D', and S2D; Movie S8), indicating a specific role for NuMA in local load-bearing and k-fiber anchorage. This partial rather than complete decrease in load-bearing may stem from residual NuMA, as expected from our cell selection protocol. Further, given the potential contribution of local k-fiber anchorage to chromosome segregation, other anchoring molecules redundant with NuMA may well also contribute. NuMA's role may either be through its own passive microtubule crosslinking ability or through its role in helping the minus-end directed motor dynein attach to microtubules as cargo [37]. The observation that the load-bearing map does not change with depleted PRC1 (Figure 4C) suggests that NuMA's role is not specific to PRC1-mediated bridging fibers.

Our work raises the question of why NuMA can locally bear the load of chromosome movement—so that its absence changes the spindle's load-bearing map—whereas other microtubule crosslinkers Eg5 and PRC1 do not detectably do so. We speculate about two possible mechanical advantages for NuMA for this function. First, Eg5 and PRC1 and/or their homologs have a preference for linking antiparallel microtubules [38–41], whereas we are unaware of any such known preference for NuMA, and indeed, NuMA's role in astral arrays implies the capability of linking parallel microtubules. Parallel microtubule crosslinking, which may thus be more efficiently mediated by NuMA than by Eg5 and PRC1, may be preferred for k-fiber anchorage. Second, NuMA exerts more friction under load directed toward the plus-end of microtubules (as would be expected in opposition to force at kinetochores) than toward the minus-end [42]; such a preference does not exist for PRC1 [42] and is, to our knowledge, unknown for Eg5. However, whether NuMA's frictional asymmetry is key to its function is not yet clear.

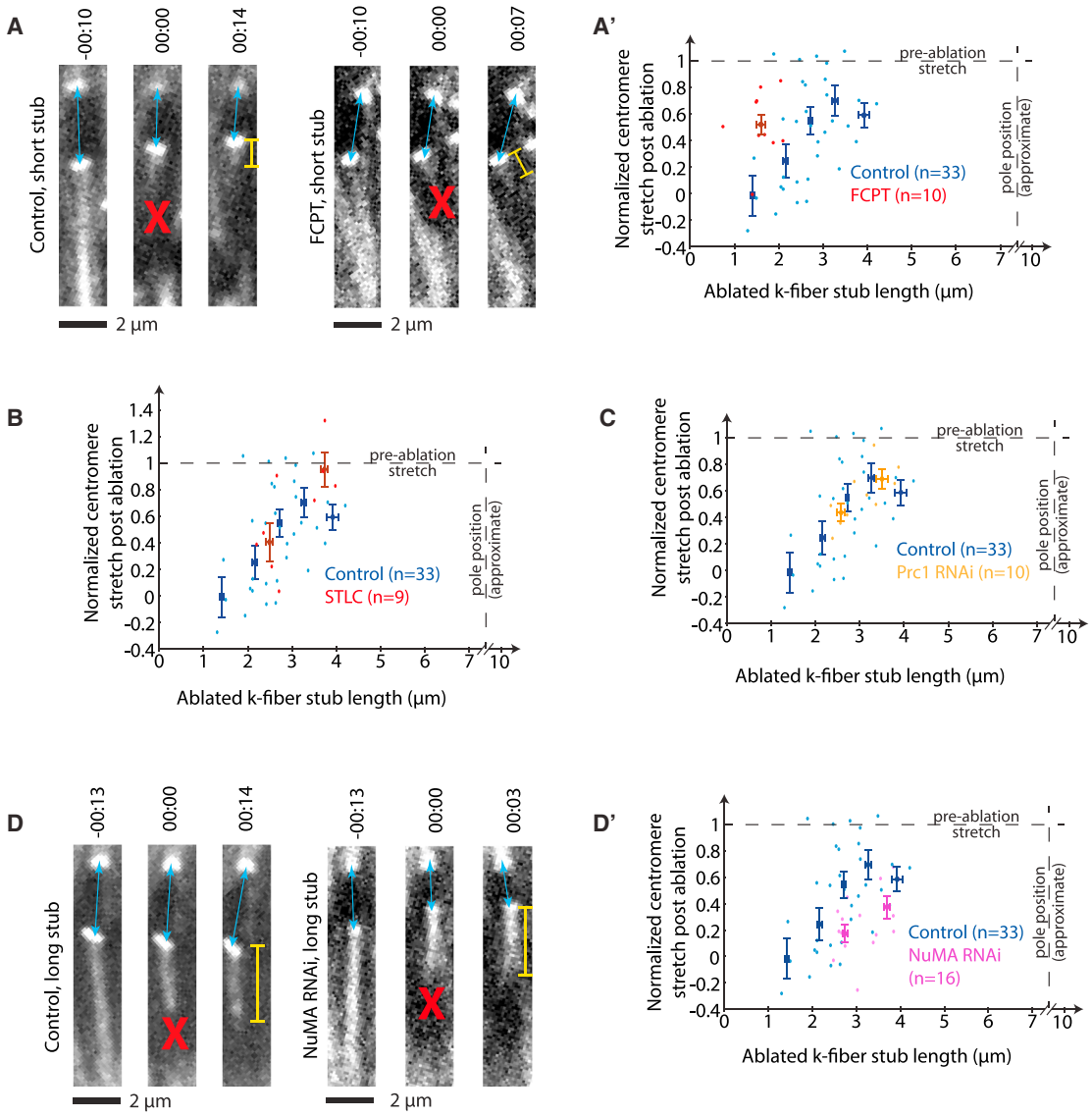

Figure 4. Local K-Fiber Anchorage Can Occur through Microtubule Crosslinking and Requires Microtubule Crosslinker NuMA, but Not Wild-Type Levels of PRC1 or Eg5

(A) Confocal live images of ablated (at red X) PtK2 cells expressing EYFP-Cdc20 and EGFP-α-tubulin. Time since ablation, min:s. Representative short k-fiber stubs (yellow bars) in a control cell (left; same movie as Figure 1C) and in a cell treated with FCPT (right) are shown. Control centromere (blue arrows) relaxes, whereas in FCPT, centromere remains stretched. (A') Normalized centromere stretch post-ablation versus k-fiber stub length for control cells (blue) and cells treated with FCPT (red) are shown, which show increased load-bearing ability for short stubs ($p = 0.04$).

(B) Normalized centromere stretch post-ablation versus k-fiber stub length for control cells (blue) and cells treated with STLC (red), which show similar load-bearing ability ($p = 0.5$).

(C) Normalized centromere stretch post-ablation versus k-fiber stub length for control cells (blue) and cells depleted of PRC1 by RNAi (gold), which show similar load-bearing ability ($p = 0.9$).

(D) Imaging as in (A). Representative long k-fiber stubs in control cell (left; same movie as in Figure 1D) and in a cell depleted of NuMA by RNAi. Control centromere (blue arrows) remains stretched, whereas in NuMA depletion, centromere relaxes. (D') Normalized centromere stretch post-ablation versus k-fiber stub length for control cells (blue) and cells depleted of NuMA by RNAi (magenta) are shown, which show a decreased load-bearing ability for long stubs ($p = 0.002$). In all graphs, light dots are individual measurements; dark dots are binned data; error bars, SEM.

See also Figure S2 and Movies S5, S6, S7, and S8.

Altogether, the data herein suggest a model where NuMA distributes the load of chromosome movement from k-fiber microtubules to nearby spindle microtubules through NuMA-based microtubule-microtubule crosslinking (Figure 5). Whereas NuMA's primary known functions have been at poles and at the cell cortex [43], our work suggests a function for NuMA within the spindle body. We propose that NuMA contributes to dense crosslinking of microtubules throughout the spindle, locally

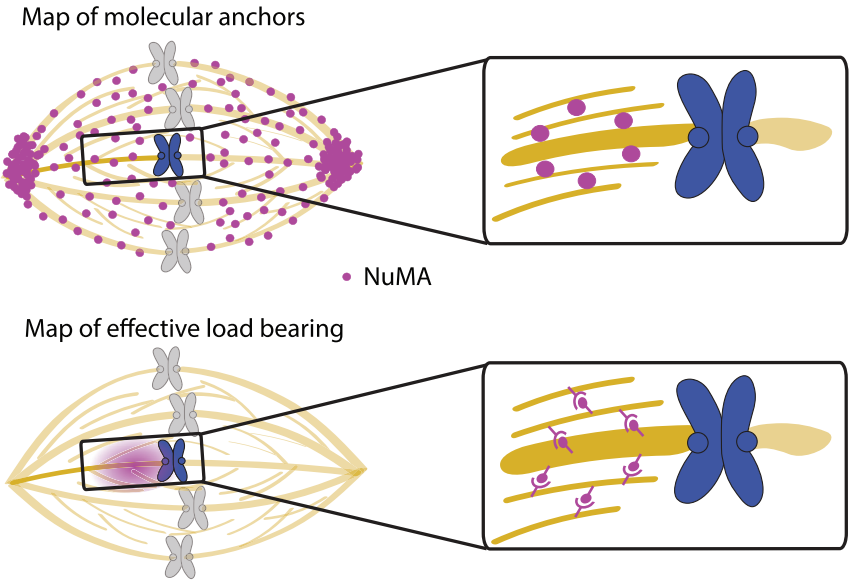

Figure 5. Model of K-Fiber Load-Bearing

The data herein suggest that widespread NuMA-mediated crosslinks in the spindle (top, purple circles) provide local load-bearing (bottom, purple cloud). Key to this model, NuMA acts in all spindle regions, locally bearing load everywhere and providing mechanical isolation and redundancy that are well suited to support robust chromosome segregation.

bearing load both around chromosomes and at poles, and mechanically isolating these from each other.

Local K-Fiber Load-Bearing Ensures Mechanical Redundancy and Robust Function

The proportionality of elastic force to k-fiber stub length and the smooth, exponential relaxation we observe over time after ablation suggest a dense network of anchoring microtubules: indeed, in a sparse network, we would instead expect discrete relaxation events as individual crosslinks ruptured. Unlike a sparser network, where each connection would be mechanically crucial, a dense network provides many local "backup" paths of force transmission for bearing the load of chromosome movement. Our data suggest that forces on chromosomes need not be transmitted all the way to poles, but whether they are remains an open question because some microtubules always remained connected to poles in our experiments. A dense microtubule network that mechanically isolates spindle regions might be particularly critical in cells where the spindle must overcome a structural defect, such as detachment of a k-fiber from the pole, or in cells undergoing physical or molecular perturbations that challenge spindle mechanics. In this way, neither connections of chromosomes to the spindle nor global spindle architecture would be jeopardized by events, such as chromosome movements, that require dynamic turnover of local connections of k-fibers to the spindle. Chromosomes must move past each other as they move to and around the metaphase plate, and the spindle must dramatically reorganize itself as it progresses through mitosis. Notably, the ability of the spindle to locally bear load implies that force generation on kinetochores, thought to, for example, stabilize kinetochore-microtubule attachments [44], is robust to distant changes in spindle architecture or forces. Thus, local and redundant load-bearing could allow the mammalian spindle to dynamically reorganize itself while preserving its ability to bear the load of chromosome movement and is well suited to support chromosome movement in species where few microtubules directly connect the kinetochore and spindle pole [45].

Looking forward, it will be important to determine whether load-bearing occurs through additional molecular mechanisms, whether and how load-bearing is regulated among different microtubule populations, and how spindle dynamics, such as poleward microtubule flux, impact local load-bearing. Finally, a key next step will be to map how load is distributed in space and time across spindles from different species and how this relates to the functions—and diverse or similar mechanical solutions—of these spindles.

STAR★METHODS

Detailed methods are provided in the online version of this paper and include the following:

- KEY RESOURCES TABLE
- CONTACT FOR REAGENT AND RESOURCE SHARING
- EXPERIMENTAL MODEL AND SUBJECT DETAILS
- METHOD DETAILS
  - Cell imaging, transfection, and siRNA
  - Small molecule treatment
  - Immunofluorescence
  - Imaging and targeted laser ablation
  - Movie preparation
  - Phenomenological model of spindle mechanics
- QUANTIFICATION AND STATISTICAL ANALYSES
  - Tracking of features of interest in live images
  - Immunofluorescence quantification
  - Statistical analysis

SUPPLEMENTAL INFORMATION

Supplemental Information includes two figures and eight movies and can be found with this article online at http://dx.doi.org/10.1016/j.cub.2017.06.018.

AUTHOR CONTRIBUTIONS

M.W.E. and S.D. designed experiments. M.W.E. and S.D. obtained preliminary data. D.B.U. designed and validated the strategy for RNAi knockdown of NuMA and PRC1 in PtK2 cells. M.W.E. performed all other experiments reported here and all analyses. M.W.E. and M.P. built the model. M.W.E. and S.D. wrote the manuscript.

ACKNOWLEDGMENTS

We thank Alexey Khodjakov for PtK2 GFP-α-tubulin cells, Jagesh Shah for PtK2 EYFP-Cdc20 cells, Marvin Tanenbaum and Ron Vale for K560-SunTag plasmids, Tim Mitchison for FCPT, and Tim Mitchison and the HMS NIC for providing support to obtain preliminary data. We thank Ron Vale; Dan Needleman; Tim Mitchison; Richard McIntosh; Ted Salmon; Megan Valentine; and Christina Hueschen, Jon Kuhn, and other members of the Dumont lab for helpful discussions. This work was supported in part by the Damon Runyon Cancer Research Foundation Fellows program (DRG-2170-13) (M.W.E.), the Keck Foundation (M.P.), NIH grants R00GM09433 and DP2GM119177 (S.D.), and the Searle Scholars Program and Rita Allen Foundation Scholars program (S.D.).

Received: January 26, 2017
Revised: May 4, 2017
Accepted: June 8, 2017
Published: July 6, 2017

REFERENCES

1. Nicklas, R.B. (1989). The motor for poleward chromosome movement in anaphase is in or near the kinetochore. J. Cell Biol. *109*, 2245–2255.
2. Waters, J.C., Mitchison, T.J., Rieder, C.L., and Salmon, E.D. (1996). The kinetochore microtubule minus-end disassembly associated with poleward flux produces a force that can do work. Mol. Biol. Cell *7*, 1547–1558.
3. Dionne, M.A., Howard, L., and Compton, D.A. (1999). NuMA is a component of an insoluble matrix at mitotic spindle poles. Cell Motil. Cytoskeleton *42*, 189–203.
4. Gordon, M.B., Howard, L., and Compton, D.A. (2001). Chromosome movement in mitosis requires microtubule anchorage at spindle poles. J. Cell Biol. *152*, 425–434.
5. Kajtez, J., Solomatina, A., Novak, M., Polak, B., Vukušić, K., Rüdiger, J., Cojoc, G., Milas, A., Šumanovac Šestak, I., Risteski, P., et al. (2016). Overlap microtubules link sister k-fibres and balance the forces on bi-oriented kinetochores. Nat. Commun. *7*, 10298.
6. Milas, A., and Tolić, I.M. (2016). Relaxation of interkinetochore tension after severing of a k-fiber depends on the length of the k-fiber stub. Matters Select, 1–13.
7. Maiato, H., Rieder, C.L., and Khodjakov, A. (2004). Kinetochore-driven formation of kinetochore fibers contributes to spindle assembly during animal mitosis. J. Cell Biol. *167*, 831–840.
8. Dumont, S., and Mitchison, T.J. (2009). Compression regulates mitotic spindle length by a mechanochemical switch at the poles. Curr. Biol. *19*, 1086–1095.
9. Hays, T.S., Wise, D., and Salmon, E.D. (1982). Traction force on a kinetochore at metaphase acts as a linear function of kinetochore fiber length. J. Cell Biol. *93*, 374–389.
10. McEwen, B.F., Heagle, A.B., Cassels, G.O., Buttle, K.F., and Rieder, C.L. (1997). Kinetochore fiber maturation in PtK1 cells and its implications for the mechanisms of chromosome congression and anaphase onset. J. Cell Biol. *137*, 1567–1580.
11. Shimamoto, Y., Maeda, Y.T., Ishiwata, S., Libchaber, A.J., and Kapoor, T.M. (2011). Insights into the micromechanical properties of the metaphase spindle. Cell *145*, 1062–1074.
12. Gatlin, J.C., Matov, A., Danuser, G., Mitchison, T.J., and Salmon, E.D. (2010). Directly probing the mechanical properties of the spindle and its matrix. J. Cell Biol. *188*, 481–489.
13. Nicklas, R.B., Kubai, D.F., and Hays, T.S. (1982). Spindle microtubules and their mechanical associations after micromanipulation in anaphase. J. Cell Biol. *95*, 91–104.
14. Matos, I., Pereira, A.J., Lince-Faria, M., Cameron, L.A., Salmon, E.D., and Maiato, H. (2009). Synchronizing chromosome segregation by flux-dependent force equalization at kinetochores. J. Cell Biol. *186*, 11–26.
15. Mastronarde, D.N., McDonald, K.L., Ding, R., and McIntosh, J.R. (1993). Interpolar spindle microtubules in PTK cells. J. Cell Biol. *123*, 1475–1489.
16. Elting, M.W., Hueschen, C.L., Udy, D.B., and Dumont, S. (2014). Force on spindle microtubule minus ends moves chromosomes. J. Cell Biol. *206*, 245–256.
17. Sikirzhytski, V., Magidson, V., Steinman, J.B., He, J., Le Berre, M., Tikhonenko, I., Ault, J.G., McEwen, B.F., Chen, J.K., Sui, H., et al. (2014). Direct kinetochore-spindle pole connections are not required for chromosome segregation. J. Cell Biol. *206*, 231–243.
18. Vladimirou, E., Mchedlishvili, N., Gasic, I., Armond, J.W., Samora, C.P., Meraldi, P., and McAinsh, A.D. (2013). Nonautonomous movement of chromosomes in mitosis. Dev. Cell *27*, 60–71.
19. Brugués, J., and Needleman, D. (2014). Physical basis of spindle self-organization. Proc. Natl. Acad. Sci. USA *111*, 18496–18500.
20. Begg, D.A., and Ellis, G.W. (1979). Micromanipulation studies of chromosome movement. I. Chromosome-spindle attachment and the mechanical properties of chromosomal spindle fibers. J. Cell Biol. *82*, 528–541.
21. Itabashi, T., Takagi, J., Shimamoto, Y., Onoe, H., Kuwana, K., Shimoyama, I., Gaetz, J., Kapoor, T.M., and Ishiwata, S. (2009). Probing the mechanical architecture of the vertebrate meiotic spindle. Nat. Methods *6*, 167–172.
22. McDonald, K.L., O'Toole, E.T., Mastronarde, D.N., and McIntosh, J.R. (1992). Kinetochore microtubules in PTK cells. J. Cell Biol. *118*, 369–383.
23. Pereira, A.J., and Maiato, H. (2012). Maturation of the kinetochore-microtubule interface and the meaning of metaphase. Chromosome Res. *20*, 563–577.
24. Tanenbaum, M.E., Gilbert, L.A., Qi, L.S., Weissman, J.S., and Vale, R.D. (2014). A protein-tagging system for signal amplification in gene expression and fluorescence imaging. Cell *159*, 635–646.
25. Cojoc, G., Roscioli, E., Zhang, L., Garcia-Ulloa, A., Shah, J.V., Berns, M.W., Pavin, N., Cimini, D., Tolić, I.M., and Gregan, J. (2016). Laser microsurgery reveals conserved viscoelastic behavior of the kinetochore. J. Cell Biol. *212*, 767–776.
26. Osswald, T., and Menges, G. (2012). Materials Science of Polymers for Engineers, Third Edition (Hanser).
27. Saxton, W.M., Stemple, D.L., Leslie, R.J., Salmon, E.D., Zavortink, M., and McIntosh, J.R. (1984). Tubulin dynamics in cultured mammalian cells. J. Cell Biol. *99*, 2175–2186.
28. Groen, A.C., Needleman, D., Brangwynne, C., Gradinaru, C., Fowler, B., Mazitschek, R., and Mitchison, T.J. (2008). A novel small-molecule inhibitor reveals a possible role of kinesin-5 in anastral spindle-pole assembly. J. Cell Sci. *121*, 2293–2300.
29. Slangy, A., Lane, H.A., d'Hérin, P., Harper, M., Kress, M., and Nigg, E.A. (1995). Phosphorylation by $p34^{cdc2}$ regulates spindle association of human Eg5, a kinesin-related motor essential for bipolar spindle formation in vivo. Cell *83*, 1159–1169.
30. Kapitein, L.C., Peterman, E.J., Kwok, B.H., Kim, J.H., Kapoor, T.M., and Schmidt, C.F. (2005). The bipolar mitotic kinesin Eg5 moves on both microtubules that it crosslinks. Nature *435*, 114–118.
31. Gaglio, T., Saredi, A., Bingham, J.B., Hasbani, M.J., Gill, S.R., Schroer, T.A., and Compton, D.A. (1996). Opposing motor activities are required for the organization of the mammalian mitotic spindle pole. J. Cell Biol. *135*, 399–414.
32. Cameron, L.A., Yang, G., Cimini, D., Canman, J.C., Kisurina-Evgenieva, O., Khodjakov, A., Danuser, G., and Salmon, E.D. (2006). Kinesin 5-independent poleward flux of kinetochore microtubules in PtK1 cells. J. Cell Biol. *173*, 173–179.
33. Polak, B., Risteski, P., Lesjak, S., and Tolić, I.M. (2017). PRC1-labeled microtubule bundles and kinetochore pairs show one-to-one association in metaphase. EMBO Rep *18*, 217–230.
34. Tolić, I.M., and Pavin, N. (2016). Bridging the gap between sister kinetochores. Cell Cycle *15*, 1169–1170.
35. Udy, D.B., Voorhies, M., Chan, P.P., Lowe, T.M., and Dumont, S. (2015). Draft de novo transcriptome of the rat kangaroo Potorous tridactylus as a tool for cell biology. PLoS ONE *10*, e0134738.

36. Tousson, A., Zeng, C., Brinkley, B.R., and Valdivia, M.M. (1991). Centrophilin: a novel mitotic spindle protein involved in microtubule nucleation. J. Cell Biol. *112*, 427–440.

37. Merdes, A., Heald, R., Samejima, K., Earnshaw, W.C., and Cleveland, D.W. (2000). Formation of spindle poles by dynein/dynactin-dependent transport of NuMA. J. Cell Biol. *149*, 851–862.

38. Subramanian, R., Wilson-Kubalek, E.M., Arthur, C.P., Bick, M.J., Campbell, E.A., Darst, S.A., Milligan, R.A., and Kapoor, T.M. (2010). Insights into antiparallel microtubule crosslinking by PRC1, a conserved nonmotor microtubule binding protein. Cell *142*, 433–443.

39. van den Wildenberg, S.M., Tao, L., Kapitein, L.C., Schmidt, C.F., Scholey, J.M., and Peterman, E.J. (2008). The homotetrameric kinesin-5 KLP61F preferentially crosslinks microtubules into antiparallel orientations. Curr. Biol. *18*, 1860–1864.

40. Loïodice, I., Staub, J., Setty, T.G., Nguyen, N.P., Paoletti, A., and Tran, P.T. (2005). Ase1p organizes antiparallel microtubule arrays during interphase and mitosis in fission yeast. Mol. Biol. Cell *16*, 1756–1768.

41. Gaillard, J., Neumann, E., Van Damme, D., Stoppin-Mellet, V., Ebel, C., Barbier, E., Geelen, D., and Vantard, M. (2008). Two microtubule-associated proteins of *Arabidopsis* MAP65s promote antiparallel microtubule bundling. Mol. Biol. Cell *19*, 4534–4544.

42. Forth, S., Hsia, K.C., Shimamoto, Y., and Kapoor, T.M. (2014). Asymmetric friction of nonmotor MAPs can lead to their directional motion in active microtubule networks. Cell *157*, 420–432.

43. Radulescu, A.E., and Cleveland, D.W. (2010). NuMA after 30 years: the matrix revisited. Trends Cell Biol. *20*, 214–222.

44. Akiyoshi, B., Sarangapani, K.K., Powers, A.F., Nelson, C.R., Reichow, S.L., Arellano-Santoyo, H., Gonen, T., Ranish, J.A., Asbury, C.L., and Biggins, S. (2010). Tension directly stabilizes reconstituted kinetochore-microtubule attachments. Nature *468*, 576–579.

45. Redemann, S., Baumgart, J., Lindow, N., Shelley, M., Nazockdast, E., Kratz, A., Prohaska, S., Brugués, J., Fürthauer, S., and Müller-Reichert, T. (2017). *C. elegans* chromosomes connect to centrosomes by anchoring into the spindle network. Nat. Commun. *8*, 15288.

46. Khodjakov, A., Copenagle, L., Gordon, M.B., Compton, D.A., and Kapoor, T.M. (2003). Minus-end capture of preformed kinetochore fibers contributes to spindle morphogenesis. J. Cell Biol. *160*, 671–683.

47. Lukinavičius, G., Reymond, L., D'Este, E., Masharina, A., Göttfert, F., Ta, H., Güther, A., Fournier, M., Rizzo, S., Waldmann, H., et al. (2014). Fluorogenic probes for live-cell imaging of the cytoskeleton. Nat. Methods *11*, 731–733.

48. Venugopalan, V., Guerra, A., 3rd, Nahen, K., and Vogel, A. (2002). Role of laser-induced plasma formation in pulsed cellular microsurgery and micromanipulation. Phys. Rev. Lett. *88*, 078103.

49. Magidson, V., Loncarek, J., Hergert, P., Rieder, C.L., and Khodjakov, A. (2007). Laser microsurgery in the GFP era: a cell biologist's perspective. Methods Cell Biol. *82*, 239–266.

50. Schindelin, J., Arganda-Carreras, I., Frise, E., Kaynig, V., Longair, M., Pietzsch, T., Preibisch, S., Rueden, C., Saalfeld, S., Schmid, B., et al. (2012). Fiji: an open-source platform for biological-image analysis. Nat. Methods *9*, 676–682.

51. Schneider, C.A., Rasband, W.S., and Eliceiri, K.W. (2012). NIH Image to ImageJ: 25 years of image analysis. Nat. Methods *9*, 671–675.

STAR★METHODS

KEY RESOURCES TABLE

REAGENT or RESOURCE	SOURCE	IDENTIFIER
Antibodies		
Mouse anti-PRC1	BioLegend	Cat# 629001; RRID: AB_2169532
Rabbit anti-α-tubulin	Sigma	Cat# T3526; RRID: AB_261659
Mouse anti-α-tubulin	Sigma	Cat# T6199; RRID: AB_477583
Rabbit anti-NuMA	Novus Biologicals	Cat# NB500-174; RRID: AB_10002562
Alexa 488 goat anti-mouse IgG	Invitrogen	Cat# A11001; RRID: AB_2534069
Alexa 488 goat anti-rabbit IgG	Invitrogen	Cat# A11008; RRID: AB_143165
Alexa 647 goat anti-mouse IgG	Invitrogen	Cat# A21236; RRID: AB_141725
Alexa 647 goat anti-rabbit IgG	Invitrogen	Cat# A21244; RRID: AB_141663
Chemicals, Peptides, and Recombinant Proteins		
SiR-tubulin dye	Spirochrome	Cat# SC-002
Verapamil	Sigma-Aldrich	Cat# V4629
Fugene 6	Promega	Cat# E2691
Oligofectamine	Invitrogen/Life Technologies	Cat# 12252011
STLC	Sigma-Aldrich	Cat # 164739
FCPT	T. Mitchison	N/A
Hoechst 33342	Sigma-Aldrich	Cat# H3570
Experimental Models: Cell Lines		
WT Ptk2 Cells	T. Mitchison	ATCC Cat# CCL-56
PtK2 GFP-α-tubulin cells	A. Khodjakov	N/A
PtK2 cells stably expressing EYFP-Cdc20	J. Shah	N/A
Oligonucleotides		
siRNA against PtK NuMA: 5′-GCATAAAGCGGAG ACUAAA-3′	[35]	N/A
siRNA against PtK PRC1: 5′-GGACTGAGGUUGU CAAGAA-3′	[35]	N/A
Recombinant DNA		
plasmid: pEGFP-tubulin	Clontech	discontinued
plasmid: K560rig-SunTag24x-GFP	Marvin Tanenbaum [24]	N/A
plasmid: scFv-GCN4-GFP	Marvin Tanenbaum [24]	N/A
Software and Algorithms		
MATLAB	MathWorks	R2013B
3D bar plot with error bars	MATLAB user lee	https://www.mathworks.com/matlabcentral/fileexchange/33225-3d-bar-plot-with-error-bars
ImageJ64	ImageJ	1.46r
Fiji	ImageJ	1.51 m
Metamorph	MDS Analytical Technologies	7.7.8.0
Other		
35 mm MatTek Dishes (poly-D-lysine coated)	MatTek Corporation	Cat# P35GC-1.5-20-C

CONTACT FOR REAGENT AND RESOURCE SHARING

Further information and requests for resources and reagents should be directed to and will be fulfilled by the Lead Contact, Sophie Dumont (sophie.dumont@ucsf.edu).

EXPERIMENTAL MODEL AND SUBJECT DETAILS

WT PtK2 cells (male kidney epithelial cells from the rat kangaroo, *Potorous tridactylus*), PtK2 GFP-α-tubulin cells (stable line expressing human α-tubulin in pEGFP-C1; Takara Bio Inc.; a gift from A. Khodjakov, Wadsworth Center, Albany, NY [46]), and PtK2 cells stably expressing EYFP-Cdc20 (gift of J. Shah, Harvard Medical School, Boston, MA) were cultured in MEM (Invitrogen) supplemented with sodium pyruvate (Invitrogen), penicillin/streptomycin, and 10% qualified and heat-inactivated fetal bovine serum (Invitrogen) at 37°C as previously described [16]. We have not authenticated these PtK2 cell lines, but our lab has previously sequenced the WT PtK2 transcriptome [35] and the results were consistent with a marsupial cell line. Furthermore, we have verified that all of these lines have expected PtK2 morphology and features.

METHOD DETAILS

Cell imaging, transfection, and siRNA

For imaging, cells were plated on 35 mm #1.5 coverslip glass-bottomed dishes coated with poly-D-lysine (MatTek) and imaged in phenol-free MEM (Invitrogen). For imaging of kinetochores and microtubules, PtK2 cells stably expressing EYFP-Cdc20 were transfected with GFP-α-tubulin using Fugene 6 (Promega) and imaged 48-72 hr post transfection. For depletion of NuMA or PRC1, ~6 hr following Fugene 6 transfection of GFP-α-tubulin, cells were also transfected with siRNA for NuMA or PRC1 using Oligofectamine (Life Technologies, Carlsbad, CA) as previously described in detail [35]. Cells were imaged 72 hr after knockdown. The following siRNAs were used: siNuMA: 5′-GCATAAAGCGGAGACUAAA-3′; siPRC1: 5′-GGACTGAGGUUGUCAAGAA-3′. PRC1 siRNA was previously validated, and siRNA for NuMA was designed from the PtK2 transcriptome as previously described [35].

For PRC1 RNAi, knockdown was previously validated in our hands by western blot [35], and was verified here by immunofluorescence (Figures S2G and S2G'). We quantified PRC1 immunfluorescence intensity in mock RNAi versus PRC1 RNAi and found average per pixel PRC1 intensity in the spindle above that in the cytoplasm of 9,700 ± 700 (AU) (SEM, n = 20) in control and 3,500 ± 700 (AU) (SEM, n = 20) in PRC1 RNAi cells (different with $p = 2x10^{-7}$). Cells used for quantification were selected based on examining the DNA channel only (so as to be unbiased for the amount of PRC1 present when selecting cells, as a control for live experiments). We also confirmed PRC1 knockdown in the particular coverslips used for live imaging by verifying at low magnification the enrichment of binucleated cells, a previously characterized consequence of PRC1 knockdown [35].

For NuMA RNAi, knockdown was verified by immunofluorescence (Figures S2G and S2G') and by spindle phenotype. We quantified NuMA intensity in mock RNAi versus NuMA RNAi and found average per pixel NuMA intensity in the spindle above that in the cytoplasm of 21,500 ± 1,800 (AU) (SEM, n = 17) in control and 3,000 ± 1,300 (AU) (SEM, n = 17) in NuMA RNAi cells (different with $p = 1x10^{-9}$). We also counted interphase cells where we were able to detect NuMA enrichment at the nucleus by eye in NuMA RNAi versus mock RNAi: 296/302 (98%) of control interphase cells had clear NuMA localization in the nucleus whereas only 10/337 (3%) of NuMA RNAi cells did, and even these nuclei with detectable NuMA appeared qualitatively to be dimmer than in control cells.

For the ablation experiments herein, we chose cells with mild signs of NuMA RNAi phenotype (e.g., longer spindles and centrosomes that did not appear fully attached), but ignored those with dramatically splayed poles or whose spindle architectures seemed otherwise significantly perturbed. In cells with mild signs of NuMA RNAi phenotype, we also quantified the time from nuclear envelope breakdown to anaphase onset by time lapse imaging at 40x magnification, and did not see a difference from control cells (t = 55+/−3 min, s.e.m, n = 37 control cells; t = 53 ± 4 min, s.e.m, n = 32 NuMA RNAi cells); this is consistent with these cells' spindles not being grossly perturbed. This similarity helps validate that the results observed herein are due to NuMA acting locally rather than a result of global perturbation of spindle architecture. The immunofluorescence quantification of NuMA fluorescence described above was performed with cells with similar spindles to those used in live cells (i.e., with only mild NuMA phenotypes). In the immunofluorescence quantification, we selected these cells based on DNA and tubulin channels only (so as to be unbiased for the amount of NuMA present when selecting cells). We saw many cells by immunofluorescence with stronger phenotypes (e.g., splayed poles and unfocused k-fibers), but did not use these for immunofluorescence (or ablation) analysis. We also confirmed NuMA knockdown in the particular coverslips used for live imaging by verifying at low magnification the enrichment of cells with disrupted spindles.

For speckle imaging of microtubules, PtK2 cells were simultaneously transfected with K560rig-SunTag24x-GFP and scFv-GCN4-GFP [24] using Fugene 6 and were imaged 72 hr after transfection. Speckle experiments required screening through many cells due to low efficiency and variable expression level of this double transfection.

Small molecule treatment

To increase microtubule crosslinking by rigor binding Eg5, we treated with 20 μM FCPT (gift of T. Mitchison, Harvard Medical School, Boston, MA) for 15-30 min. Under these conditions, flux was slowed to 0.1 ± 0.1 μm/min (SEM, n = 5) versus 0.8 ± 0.1 μm/min in control cells (SEM; n = 10), but chromosomes still oscillated, indicating that spindle crosslinking was increased but that spindles remained dynamic (allowing us to normalize for centromere stretch over an oscillation cycle as described).

To inhibit Eg5 motor activity, we treated with 5 μM S-trityl-L-cysteine (STLC, Sigma) in MEM for 30 min, and chose cells that remained bipolar, indicating that they entered mitosis before drug treatment began [32]. Under these conditions, we observed many monopolar spindles, which indicated that the drug treatment effectively inhibited Eg5.

For speckle experiments, we used SiR-tubulin (alongside speckle strategy described above) to visualize microtubules [47]. We treated with 10 μM verapamil and 100 nM SiR-tubulin (Spirochrome) for 2-6 hr to allow time for incorporation of SiR-tubulin into spindles. Under these conditions, there was no detected defect in spindle appearance or behavior.

Immunofluorescence

For examining the presence of PRC1 or NuMA following depletion by RNAi, the following antibodies were used: mouse anti-PRC1(1:100, BioLegend), rabbit anti-α-tubulin (1:200, Sigma), mouse anti-α-tubulin DM1α (1:1000, Sigma), rabbit anti-NuMA (1:300, Novus Biologicals), fluorescent secondary antibodies (1:500, Invitrogen), and Hoechst 33342 (Sigma). Cells were fixed with 95% methanol with 5 mM EGTA for 3 min.

Imaging and targeted laser ablation

As previously described [16], live imaging was performed on a Nikon Eclipse Ti-E inverted microscope with a Yokogawa CSU-X1 spinning disk confocal; head dichroic Semrock Di01-T488 (except Di01-T405/488/568/64 for speckle experiments with SiR-tubulin and Di01-T405/488/561for immunofluorescence); 405 nm (100 mW), 488 nm (120 mW), 561 (150 mW) and 642 nm (100 mW) diode lasers; emission filters Chroma ET455/50M, ET520/20M, ET 525/50M, ET630/75M, and ET690/50M; and an Andor iXon3 camera. Cells were imaged via Metamorph (7.7.8.0, MDS Analytical Technologies) by phase contrast (400 ms exposures) and fluorescence (75-400 ms exposures) with a 100X 1.45 Ph3 oil objective through a 1.5X lens yielding 105 nm/pixel at bin = 1. Cells were imaged every 3-7 s or, in the case of fast speckle imaging, the camera was used in continuous streaming mode for 20-30 frames. Cells were imaged at 29-31°C and 5% CO2 in a Tokai Hit scope top incubator, using the Nikon Perfect Focus System. Targeted laser ablation (20-30 3 ns pulses at 20 Hz) using 551 nm light was performed using a galvo-controlled MicroPoint Laser System (Photonic Instruments) operated through Metamorph. Calibration of MicroPoint galvo targeting was done each day before imaging by targeted ablation on an aluminum-coated mirror slide. Based on fluorescence imaging, we estimate the diameter of the ablation site at approximately 1 μm. The precise physical mechanism by which laser ablation destroys cellular structures is not well understood, though there is evidence that ns-pulsed lasers may induce a localized plasma and subsequent cavitation bubble that leads to destruction of local structures [48]. Whatever its mechanism, ablation with such laser systems is reliably able to destroy organelles in a targeted region whose size is confined by at least the Rayleigh criterion or smaller [49]. K-fiber ablation was verified by observed loss of tension across the centromere and/or depolymerization of the uncapped microtubule plus-ends created by k-fiber severance. Except in the case of fast imaging (Figures 2C and 2D; Figures 3A–3C), we set time = 0 at the first frame following the conclusion of ablation. In the case of fast imaging, images are taken continuously, so that t = 0 is set to the beginning of ablation. Ablation itself takes ~1-1.5 s.

Movie preparation

In order to detect the details of the cellular response to ablation while minimizing photodamage from frequent imaging, cells were imaged less frequently before ablation and more frequently immediately following ablation, but play back at a constant 5 fps. ImageJ was used to add scale bars, timestamps, and other labels to the movies.

Phenomenological model of spindle mechanics

The following simple free body diagram depicts the conceptual framework for force balance on the kinetochore (indicated by the '*'). On the left is the centromere, represented as a Kelvin-Voigt viscoelastic solid with an effective viscosity η_{cent} and stiffness k_{cent}. We consider the sister kinetochore (left, attached to the uncut k-fiber, not shown) to be fixed during the time period we observe. On the right is the k-fiber stub of length, L. The mechanical connections of this stub to the spindle are represented as crosslinking bonds and viscous drag of the stub in the spindle. We model the crosslinking bonds as "on/off bonds" that can each exert force up to a maximum force f_o before rupturing. These crosslinks are present at a number density N_0 per unit length. The term η_{MT} accounts for a length-dependent viscous drag of the k-fiber stub in the spindle environment. Finally, Δx_{cent} represents the stretch of the centromere beyond its relaxed distance. The change in Δx_{cent} following ablation is also equal to the displacement of the k-fiber stub, which is assumed to be stiff with respect to the applied forces. We have chosen a convention where positive Δx_{cent} (i.e., centromere stretch) goes to the right in this diagram. We assume that this is a system with small strain, that can hence be approximated by linear springs and viscous dashpots with Newtonian composition.

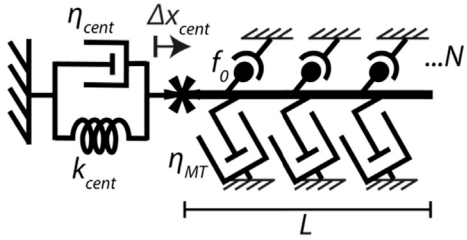

Pre-ablation, the system is in a stretched state, with the amount of stored stress indicated by the distance across the centromere. Post-ablation, the system relaxes with a given timescale (τ). We assume this timescale comes both from the viscous drag of the k-fiber stub and dissipation in the contracting chromosome. As inertia is not important in this system, and we assume small

displacements in linear regime of the spring, we can equate the stress on the centromere to the net force experienced by the stiff k-fiber stub (at all times). Since we assume the k-fiber stub (modeled as a stiff rod of length L moving through the spindle) does not change length, the change in distance across the centromere in response to ablation is equal to the deflection of the k-fiber stub. Thus, matching the stresses (σ) for the centromere, on the left, and the k-fiber-to-spindle mechanics, on the right, gives the following equation:

$$\sigma = k_{cent}(-\Delta x_{cent}) - \eta_{cent}\frac{d(\Delta x_{cent})}{dt} = -N_0 L f_0 + L\eta_{MT}\frac{d(\Delta x_{cent})}{dt}.$$

Thus, simplifying:

$$k_{cent}(-\Delta x_{cent}) = -N_0 L f_0 + (L\eta_{MT} + \eta_{cent})\frac{d(\Delta x_{cent})}{dt}.$$

The solution to this equation of motion is a single exponential, given by:

$$\Delta x_{cent}(t) = \frac{N_0 L f_0}{k_{cent}} + Ae^{-t/\tau}$$

where

$$\tau = \frac{L\eta_{MT} + \eta_{cent}}{k_{cent}}$$

and

$$A = \Delta x_0 - \frac{N_0 L f_0}{k_{cent}}$$

with an initial condition of $\Delta x_{cent} = \Delta x_0$ at time $t = 0$, when ablation occurs. We simplify these by defining:

$$\Delta x' = \frac{N_0 L f_0}{k_{cent}}$$

and

$$L_0 = \frac{k_{cent}\Delta x_0}{N_0 f_0}$$

where $\Delta x'$ describes the extention that can be sustained by a stub length L, and L_0 describes the stub length that can sustain the extension Δx_0. However, the crosslinking bonds can exert *up to* a force f_0, but will only exert enough force to oppose that from the stretched centromere. Thus, once the k-fiber stub is sufficiently long to fully oppose the stretched centromere, $k_{cent}\Delta x_{cent}$, then there will no longer be any relaxation following ablation, and the force exerted by the crosslinkers will not go above the force necessary to oppose the stretch from the centromere. To account for this, it is thus necessary to define $\Delta x_{cent}(t)$ in a piecewise manner with respect to the stub length, L. For that reason, we find the complete solution:

$$\Delta x_{cent}(t) = \begin{cases} \Delta x' + Ae^{-\frac{t}{\tau}}, \ when\ L < L_0 \\ \Delta x_0, \ when\ L \geq L_0 \end{cases}$$

QUANTIFICATION AND STATISTICAL ANALYSES

Tracking of features of interest in live images

K-fiber ends and spindle pole positions were tracked manually on either EYFP-Cdc20 and EGFP-α-tubulin or EGFP-α-tubulin alone images in home-written MATLAB (R2012a/R2016a) programs. Length of k-fiber stubs were calculated as the distance from the tracked k-fiber ends to the coordinate position of the center of MicroPoint targeting (see above). Post-ablation relaxation was calculated as the minimum measured distance between k-fiber ends in the period immediately following ablation. To account for possible variation in centromere stiffness across chromosomes and in stretch at the time of ablation, distance across the centromere was normalized as depicted in Figure 1E, and we followed chromosomes for long enough to observe the minimum centromere distance of at least one oscillation cycle before ablation to allow normalization to the minimum stretch during a normal oscillation. We then waited until near maximal centromere stretch to ablate to maximize our dynamic range. For normalized centromere stretch graphs (Figures 1F, 2A, and 4), data were binned into equal width bins by k-fiber stub length. For neighboring chromosomes (Figures 2B and S1A), we were not able to ablate at the time of maximal stretch since neighboring chromosomes were not necessarily in phase with the chromosome whose k-fiber we were targeting. Since there is no detectable mean decrease in centromere distance (and thus the change in centromere stretch is dominated by the oscillation cycle), the change in centromere distance is sometimes positive and sometimes negative.

For speckle imaging, speckles to track were manually chosen, and were tracked using the centroid for subpixel localization, also in a home-written MATLAB program. During tracking, intensity was adjusted to optimize for tracking dim speckles, but in Movie S3, it has been adjusted to prevent saturation of brighter speckles, making some tracked speckles appear dim in this movie. All analysis based on these positions and plots were created with home written MATLAB programs. To align traces on top of each other, a pole-to-pole axis was created by manually recording the positions of the poles, and spindle coordinates of speckles were aligned so that the position of ablation was set to (0,0) and rotated so that the pole-to-pole axes were parallel and the position of the corresponding chromosome had a positive x-value. MATLAB was used to plot these aligned traces on top of each other (Figure 2D) and color these traces according to their lengths. MATLAB function ThreeDErrorBars.m from user lee was used to create the 3D histogram (Figure 3E). For calculating p values of distances moved quoted in the text, the measurements from the bin in this figure that goes from 0 to 2 μm along the x axis and from -1 to 1 μm along the y axis were compared using an unpaired t test to measurements from all the surrounding bins (each 2 μm wide) together. To create the time-to-color projection in Figure 2C, we used the Temporal-Color Code plugin in Fiji [50].

Kymograph of fast relaxation (Figure 3) was created in ImageJ [51]. Relaxation traces were fit as in Figure 3B by fixing the mean position before ablation at 0 and fitting the total magnitude of the movement A and the timescale τ to a single exponential function. Most of the traces fit well to single exponentials, but a few outlier traces, which had average length stubs, did not, possibly due to incomplete ablation or failure to reach steady state before the engagement of the poleward transport force.

To measure poleward flux, we photobleached k-fibers in PtK2 EGFP-α-tubulin cells using lower power settings of the MicroPoint system and manually tracked the location of photobleached spots over time in a home-written MATLAB program. Average flux speed was calculated as the distance moved between the first and last tracked point.

Immunofluorescence quantification

For NuMA linescan analysis of immunofluorescence images, we created ROIs in ImageJ along k-fibers using staining for tubulin and measured the intensity of both tubulin and NuMA staining using ImageJ. We took the ratio of NuMA to tubulin for each k-fiber and then took the mean of all k-fibers measured as a function of the distance along the k-fiber.

We used ImageJ to calculate per pixel intensity of PRC1 and NuMA staining on spindles for verifying RNAi.

Statistical analysis

We use unpaired t test (function ttest2 in MATLAB) for calculating p values throughout. ''Significance'' was classified as $p < 0.05$. As described in the text, we did not collect ablation data for the full stub length range for each molecular perturbation (Figure 4), but instead concentrated on the range (short or long stub lengths) for which we expected the greatest effect for that particular perturbation. Thus, to allow for a fair comparison for calculating p values, we compared the entire dataset for each molecular perturbation to the subset of control data that overlapped with the same range of stub lengths where that particular perturbed dataset was collected.

Error bars throughout are calculated as standard error of the mean. Quoted n's are described in more detail where mentioned in the text, but in general refer to individual measurements (e.g., individual chromosomes, speckles, spindles, etc.).